# Limit Cycle Analyses of Extended EMF-Based Position-Sensorless in IPMSM Drives

Xinghao Wang, *Graduate Student Member, IEEE*, Dehui Luo, *Graduate Student Member, IEEE*, and Dianxun Xiao, *Member, IEEE*

***Abstract*—This article reveals a limit cycle issue in the widely used position estimation method of interior permanent magnet synchronous motors (IPMSMs) based on extended back electromotive force (EMF). The limit cycle can result in self-oscillations in the estimated rotor position and greatly increase the estimation errors. In this article, a nonlinear model is proposed to analyze the arctangent nonlinearity involved in the EMF method, and a describing function approach is employed to derive the critical criteria for limit cycle issue. The result shows that a limit cycle will be excited when the parameters of the phase-locked loop exceed the critical value. The parameter boundary is determined by the operating conditions and motor parameters, which facilitates the tuning of sensorless control. Theoretical analyses are verified on the IPMSM setup, of which experimental results confirm the correctness of the proposed analysis in predicting the autonomous oscillation in extended EMF-based position estimation.**

***Index Terms*—Describing function, extended back electromotive force (EMF), interior permanent magnet synchronous motor (IPMSM), limit cycle, position-sensorless control.**

## I. Introduction

INTERIOR permanent magnet synchronous motors (IPMSMs) attract a great deal of attention in the industry due to their high efficiency, low torque ripple, and wide speed range [1]. Position-sensorless control shows competitive advantages in IPMSM drives, including cost savings, volume reduction, and fault-tolerance capability. Therefore, numerous sensorless control strategies have been proposed in the literature and successfully applied in industrial applications, such as transportation and home appliances [2], [3], [4]. Throughout the development of sensorless control, most of the aspects and problems have been well analyzed and addressed, but there are still some issues, which are previously ignored and should be further explored.

Low-speed position sensorless control is often based on high-frequency (HF) injection, which utilizes the anisotropy of the magnetic field to estimate the position of the rotor by injecting a series of HF signals [5], [6], [7], [8]. The method can offer a high accuracy of estimation if the saliency of the rotor of the IPMSM is apparent. In addition to HF injection, a random frequency injection-based scheme can be used to reduce acoustic noise caused by conventional HF injection signals [9], [10], [11]. However, the injection-based methods are unavailable for high-speed sensorless control, due to the dc-link voltage limit for injection-based methods and the narrow region for zero-vector detection.

Model-based methods can be used for high-speed position estimation of the IPMSM, which includes active flux estimation [12], [13], [14] and back electromotive force (EMF) estimation [15], [16], [17], [18], [19], [20], [21], [22], [23], [24], [25], [26], [27], [28], [29], [30] [31], [32], [33], [34]. Due to the lower sensitivity to parameter mismatches and current measurement offsets, EMF estimation is more general than the active flux method. For IPMSM drives, the extended EMF is estimated for position-sensorless control [15].

Many research efforts are focused on the accuracy improvement of the extended EMF-based estimation method. Voltage distortions caused by the inverter nonlinearity were reported as the main causes of periodic position estimation errors [18]. Due to only the reference voltage being used in estimation, primary fifth and seventh harmonic errors between the reference voltage and output voltage can result in sixth-order position errors. To suppress the harmonic fluctuation, advanced position observers have been proposed in the literature recently [18], [19], [20], [21], [22]. Meanwhile, parameter mismatch and asymmetry can also cause the estimated position error. Therefore, the solutions to improve the accuracy of the estimated position are summarized in Table I. Moreover, the iron loss is considered in the extended EMF model in [32] for an ultra-high-speed IPMSM drive. A discrete extended EMF modeling approach at a low carrier-to-fundamental frequency ratio was

Received 28 July 2024; revised 12 October 2024 and 24 November 2024; accepted 22 December 2024. Date of publication 1 January 2025; date of current version 26 February 2025. This work was supported in part by the National Natural Science Foundation of China under Grant 52307069, in part by the Guangdong Basic and Applied Basic Research Foundation under Grant 2022A1515140050, in part by the Guangzhou Science and Technology Program under Grant 2023A03J0653 and Grant 2023A04J1034, in part by the Guangdong Featured Innovation Project of General College and University under Grant 2023KTSCX168, in part by the 2024 Tertiary Education Scientific Research Project of Guangzhou Municipal Education Bureau under Grant 2024312176, and in part by the Project of Hetao Shenzhen-Hong Kong Science and Technology Innovation Cooperation Zone under Grant HZQB-KCZYB 2020083. Recommended for publication by Associate Editor A. J. Marques Cardoso. *(Corresponding author: Dianxun Xiao.)*

Xinghao Wang and Dehui Luo are with the Sustainable Energy and Environment Thrust, The Hong Kong University of Science and Technology (Guangzhou), Guangzhou 511457, China (e-mail: xwang219@connect.hkust-gz.edu.cn; dluo851@connect.hkust-gz.edu.cn).

Dianxun Xiao is with the Sustainable Energy and Environment Thrust, The Hong Kong University of Science and Technology (Guangzhou), Guangzhou 511457, China, and also with HKUST Shenzhen–Hong Kong Collaborative Innovation Research Institute, Shenzhen 518048, China (e-mail: dianxunxiao@hkust-gz.edu.cn).

Color versions of one or more figures in this article are available at https://doi.org/10.1109/TPEL.2024.3524793.

Digital Object Identifier 10.1109/TPEL.2024.3524793

TABLE I
SOLUTIONS OF ESTIMATION HARMONIC IN SENSORLESS CONTROL

| Problems | Harmonic Order | Solution |
|---|---|---|
| Inverter nonlinearity | Sixth order | [16], [17], [18], [19], [20], [21], [22] |
| Parameter mismatch | DC offset | [23], [24], [25], [26], [27], [28] |
| Parameter asymmetry | Dc offset and Second order | [23], [29], [30], [31] |

analyzed in [33]. In consequence, by taking these nonideal factors into consideration, the extended EMF-based method has proven to be an effective approach for high-speed sensorless control.

However, there is still an issue that has not been explored well, which is the speed estimation error. The extended EMF model exhibits nonlinearity due to rotor saliency, which involves a speed-related term in the model. Since the actual speed is unknown, the estimated speed is used in various types of estimators with the assumption that the speed estimation error is zero [15], [16], [17], [18], [19], [20], [21], [22], [23], [24], [25], [26], [27], [28], [29], [30] [31], [32], [33], [34]. The assumption simplifies the nonlinear estimator to a linear model, consequently resulting in the loss of modeling accuracy. The dynamic and nonlinear characteristics of the estimator cannot be reflected in the conventional linear model. As reported in [34], ignoring the speed estimation error in the estimator will lead to large estimation errors in the transient state. An enhanced position and speed estimator were therefore proposed to improve the dynamic performance. Nonetheless, research on the effects of speed estimation errors is still limited in the literature.

In this article, a serious limit cycle phenomenon is found in the extended EMF-based position estimation method due to the speed estimation error. The limit cycle leads to autonomous oscillations in the position estimation, which are self-excited and sustained. It can significantly increase the position estimation error and cause the sensorless control to be unstable in load conditions. However, conventional analyses on the position estimation of IPMSM use an approximate linear model and assume no errors between the actual and estimated speed, which cannot obtain theoretical analyses for this nonlinear phenomenon. Therefore, a novel nonlinear modeling method considering the speed error is used in this article to analyze the adverse impact of speed estimation errors on the position estimator. The analysis shows that a nonlinear feedforward path with arctangent nonlinearity is involved in position estimation, which has not been found in the literature. Through the describing function method [35], the nonlinear characteristic of the position estimation can be analyzed, and the critical condition of exciting the limit cycle is obtained. To avoid the self-sustained oscillation in position estimation, the parameter of the PLL should be tuned smaller than the critical value, which is a function of operating conditions. The correctness of theoretical analyses was verified on an IPMSM drive. The main contributions of this article are summarized as follows.

1) Revelation of a serious limit cycle phenomenon in the extended EMF-based position estimation method of IPMSMs due to speed estimation errors, leading to self-
2) Discovery of a nonlinear feedforward path with arctangent nonlinearity involved in position estimation considering speed estimation errors, a finding not previously reported in the literature.
3) Application of the describing function method to analyze the nonlinear characteristic of the position estimation and to determine the critical condition for exciting the limit cycle.
4) Practical recommendation to tune the PLL parameter with the verification of theoretical analyses on an IPMSM drive.

## II. MODELING OF THE EXTENDED EMF-BASED POSITION ESTIMATION METHOD

### A. Conventional Model Without Speed Errors

Medium–high speed position-sensorless control of the IPMSM is often based on the extended EMF method. The IPMSM model can be expressed in $\alpha\beta$-axes, given as follows:

$$\boldsymbol{u}_{\alpha\beta} = (pL_d + R_s)\boldsymbol{i}_{\alpha\beta} + \boldsymbol{e}_{\alpha\beta} + j\omega_e \Delta L \cdot \boldsymbol{i}_{\alpha\beta} \tag{1}$$

where $\boldsymbol{u}_{\alpha\beta}$ and $\boldsymbol{i}_{\alpha\beta}$ are the stator voltages and currents, respectively, $R_s$ is the stator resistance, $L_d$ and $L_q$ are the $dq$-axes stator inductances, $\Delta L = L_q - L_d$ is the inductance difference, $\boldsymbol{e}_{\alpha\beta}$ is the extended EMF, $\omega_e$ is the electrical rotor frequency, $p$ is the differential operator, and $j$ is the imaginary index.

The extended EMF can be expressed as

$$\boldsymbol{e}_{\alpha\beta} = -E_x(\sin\theta_e - j\cos\theta_e) \tag{2}$$

where $E_x = \Delta L(pi_d - \omega_e i_d) + \omega_e \varphi$, $\theta_e$ is the rotor position, and $\varphi$ is the flux linkage.

As observed in (2), the extended EMF contains information on the position of the rotor. For position-sensorless control, the extended EMF can be directly calculated from the IPMSM model [36], [37], [38], given as follows:

$$\hat{\boldsymbol{e}}_{\alpha\beta} = \boldsymbol{u}^{\text{ref}}_{\alpha\beta} - (pL_d + R_s)\boldsymbol{i}_{\alpha\beta} - j\hat{\omega}_e \Delta L \cdot \boldsymbol{i}_{\alpha\beta} \tag{3}$$

where $\hat{\bullet}$ denotes estimated variables, and the superscript (ref) in $\boldsymbol{u}^{\text{ref}}_{\alpha\beta}$ represents the reference voltage.

Compared with the IPMSM model in (1), the reference voltage and the estimated speed are used in the estimator (3), instead of the actual values that should be measured by sensors. The use of the reference voltage can result in sixth harmonics in the estimated EMF due to the inverter nonlinearity. However, the impact of the estimated speed on the estimator is seldom concerned, and an approximation of $\hat{\omega}_e = \omega_e$ is often used in the conventional method to simplify the analysis [30], [31], [32], [33], [34], [35], [36].

Afterward, the rotor position can be estimated from the estimated EMF by a phase-locked loop (PLL) [39], as shown in Fig. 1. In the PLL, an equivalent position error $\varepsilon$ is calculated by the heterodyne method. A normalization scheme is employed to remove the EMF magnitude and derives a normalized position error $\varepsilon_{\text{norm}}$, given as follows:

$$\varepsilon_{\text{norm}} \approx \frac{-\hat{e}_\alpha \cos\hat{\theta}_e - \hat{e}_\beta \sin\hat{\theta}_e}{\sqrt{\hat{e}_\alpha^2 + \hat{e}_\beta^2}} \approx \frac{E_x \sin(\theta_e - \hat{\theta}_e)}{E_x} \approx \theta_e - \hat{\theta}_e. \tag{4}$$

After the $\varepsilon_{\text{norm}}$ converges to zero through the proportional–

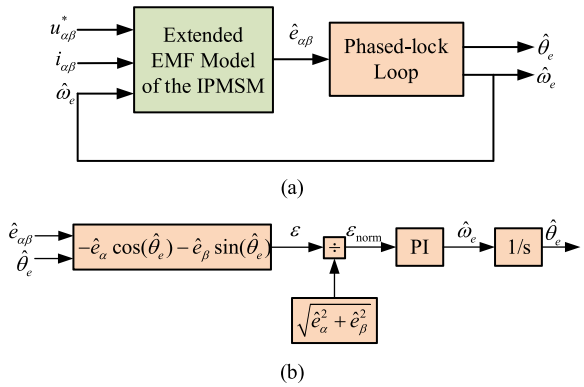


Fig. 1. Structure of the extended EMF-based estimator with a PLL. (a) Overall structure of the estimator. (b) Structure of the PLL.

However, the model derived from (1) to (3) is inaccurate due to the assumption of $\hat{\omega}_e = \omega_e$. The speed error is often larger than the position error and cannot be ignored directly. The EMF estimator in (3) becomes a nonlinear system due to the presence of the estimated speed, and its nonlinear characteristic has not been explored in the literature. In order to improve the accuracy of position estimation, the nonlinear estimator should be analyzed.

### B. Nonlinear Model With Speed Errors

In this section, the speed estimation error is considered in the EMF estimation. By comparing (1) and (3), due to $\omega_e \neq \hat{\omega}_e$, thus, the estimated EMF can be obtained as

$$\hat{\boldsymbol{e}}_{\alpha\beta} = \boldsymbol{e}_{\alpha\beta} + j(\omega_e - \hat{\omega}_e)\Delta L \cdot \boldsymbol{i}_{\alpha\beta} \tag{5}$$

where the voltage error between the reference and actual voltages is not included, since its effect has been well analyzed in the literature as mentioned before. Hence, only the speed estimation error is considered in the modeling to avoid redundancy.

Based on (5), $\hat{e_\alpha}$ and $\hat{e_\beta}$ are expressed as

$$\begin{cases} \hat{e}_\alpha = e_\alpha - (\omega_e - \hat{\omega}_e)\Delta L \cdot i_\beta \\ \hat{e}_\beta = e_\beta + (\omega_e - \hat{\omega}_e)\Delta L \cdot i_\alpha \end{cases} \tag{6}$$

where

$$\begin{cases} e_\alpha = -E_x \sin\theta_e \\ e_\beta = E_x \cos\theta_e. \end{cases}$$

According to Fig. 1, the equivalent position error $\varepsilon$ before normalization can be obtained by substituting (6) into the PLL, which is given as

$$\begin{aligned} \varepsilon &= -\hat{e}_\alpha \cos\hat{\theta}_e - \hat{e}_\beta \sin\hat{\theta}_e \\ &= E_x \sin(\theta_e - \hat{\theta}_e) + (\omega_e - \hat{\omega}_e)\Delta L \cdot H_e \end{aligned} \tag{7}$$

where

$$H_e = i_\beta \cos\hat{\theta}_e - i_\alpha \sin\hat{\theta}_e$$

where the first term is the same as the conventional model given in (4), while the second term is generated by the speed estimation error.

In (7), $\boldsymbol{i}_{\alpha\beta}$ can be replaced by $\boldsymbol{i}_{dq}$ by Park's transformation: $i_\alpha = i_d \cos\theta_e - i_q \sin\theta_e$ and $i_\beta = i_d \sin\theta_e + i_q \cos\theta_e$. Thus, substituting $\boldsymbol{i}_{dq}$ into $H_e$, given as follows:

$$H_e = i_d \cdot \sin(\theta_e - \hat{\theta}_e) + i_q \cdot \cos(\theta_e - \hat{\theta}_e). \tag{8}$$

After some derivation, the equation (7) can be rewritten as

$$\varepsilon = E'_x \sin(\theta_e - \hat{\theta}_e) + (\omega_e - \hat{\omega}_e)\Delta L \cdot i_q \cos(\theta_e - \hat{\theta}_e) \tag{9}$$

where

$$E'_x = E_x + (\omega_e - \hat{\omega}_e)\Delta L \cdot i_d.$$

By assuming

$$\begin{cases} \sin\mu = \dfrac{(\omega_e - \hat{\omega}_e)\Delta L \cdot i_q}{\sqrt{E'^2_x + (\omega_e - \hat{\omega}_e)^2 \Delta L^2 \cdot i_q^2}} \\ \cos\mu = \dfrac{E'_x}{\sqrt{E'^2_x + (\omega_e - \hat{\omega}_e)^2 \Delta L^2 \cdot i_q^2}}. \end{cases} \tag{10}$$

The model (9) can be further simplified after trigonometric operation, which gives

$$\varepsilon = \sqrt{E'^2_x + (\omega_e - \hat{\omega}_e)^2 \Delta L^2 \cdot i_q^2}\, \sin(\theta_e - \hat{\theta}_e + \mu) \tag{11}$$

where

$$\begin{aligned} \mu &= \tan^{-1}\left[\frac{(\omega_e - \hat{\omega}_e)\Delta L \cdot i_q}{E'_x}\right] \approx \tan^{-1}\left[\frac{(\omega_e - \hat{\omega}_e)\Delta L \cdot i_q}{E_x}\right] \\ &= \tan^{-1}\left[m \cdot (\omega_e - \hat{\omega}_e)\right] \end{aligned} \tag{12}$$

where the $E'_x$ in denominator of the signal phase (12) can be approximated by the extended EMF $E_x$, as $|E_x| \gg |(\omega_e - \hat{\omega}_e)\Delta L \cdot i_d|$ holds for high-speed sensorless control. A new variable $m$ is introduced in (12) to simplify the expression, which can be approximately written considering the steady state as

$$m = \frac{\Delta L \cdot i_q}{E_x} = \frac{\Delta L \cdot i_q}{\Delta L(p i_d - \omega_e i_d) + \omega_e \varphi} \approx \frac{\Delta L \cdot i_q}{\omega_e(\varphi - \Delta L \cdot i_d)}. \tag{13}$$

Similar to the conventional position estimation model, the magnitude in (11) can also be removed by the normalization scheme in the PLL. The magnitude is calculated by the square root of the estimated EMF in (5), and the normalized equivalent position error $\varepsilon_{\text{norm}}$ will be derived as

$$\varepsilon_{\text{norm}} = \sin(\theta_e - \hat{\theta}_e + \mu) \approx \theta_e - \hat{\theta}_e + \mu. \tag{14}$$

Compared with the conventional model in (4), which ignores the speed error, an additional phase $\mu$ is introduced in the proposed model due to the speed error $\omega_e - \hat{\omega}_e$. The phase $\mu$ is related to the rotor saliency $\Delta L$, flux linkage $\varphi$, and operating conditions, such as $\boldsymbol{i}_{dq}$ and $\omega_e$, according to (12) and (13). In other words, the impact of the speed error does not exist in surface-mounted PMSMs or IPMSMs with $i_q = 0$.

To illustrate the impact of speed errors, the small-signal models of the typically used position estimation expressed by (4), and the actual estimator expressed by (14) is given in Fig. 2. The conventional estimator model ignoring speed errors is a linear system, as shown in Fig. 2(a). However, due to the presence of the speed error, an additional nonlinear path is introduced in Fig. 2(b). The feedforward path contains a derivative operator of the position error $\theta_e - \hat{\theta}_e$ and a nonlinear function $\tan^{-1}(\bullet)$, which is modeled by (14).

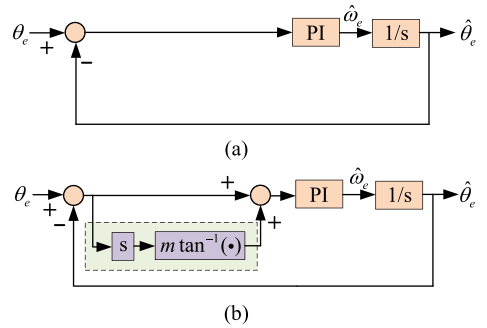


Fig. 2. Small-signal models of EMF-PLL-based position estimators. (a) Conventional linear model. (b) Nonlinear model.

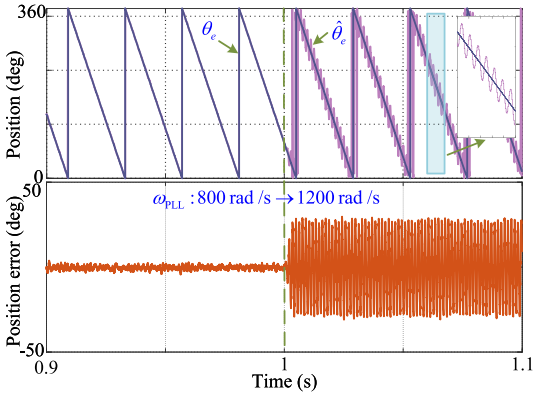


Fig. 3. Numerical verification of the limit cycle issue.

TABLE II
PARAMETERS OF THE PMSM TEST BENCH

| Parameters | Values | Parameters | Values |
|---|---|---|---|
| Rated Power | 56 W | Rated Speed | 1000 r/min |
| Pole Pairs | 5 | Rated Current | 0.25 A |
| $d$-axis inductance | 180 mH | q-axis inductance | 250 mH |
| Flux Linkage | 0.135 Wb | Stator Resistance | 37.75 Ω |

To demonstrate the influence of the nonlinear system, the position estimation result in a simulation is presented in Fig. 3. Motor parameters are given in Table II in the experimental section. The parameters of the PLL in Fig. 2 are calculated by

$$k_p = 2\omega_{\text{PLL}}, k_i = \omega_{\text{PLL}}^2 \tag{15}$$

which are the widely used parameter design schemes in the literature [40], [41]. In (15), the $\omega_{\text{PLL}}$ presents the pole location and natural frequency of the PLL.

In simulation verification, IPMSM runs at −500 r/min, and $\boldsymbol{i}_{dq}$ is −0.1 A and 0.25 A, respectively. Before 1 s, the $\omega_{\text{PLL}}$ is equal to 800 rad/s. After 1 s, the $\omega_{\text{PLL}}$ is increased to 1200 rad/s, and other conditions remain the same. As shown, with a lower $\omega_{\text{PLL}}$, the rotor position is well estimated. However, when $\omega_{\text{PLL}}$ is higher, the estimated position of the extended EMF-based estimator has large oscillations. The oscillation is not induced by noises due to such an ideal simulation scenario. The frequency and amplitude of oscillations remain unchanged in the steady state, thus being an autonomous oscillation, also called a self-sustained oscillation. The autonomous oscillation issue is caused by limit cycles in control systems.

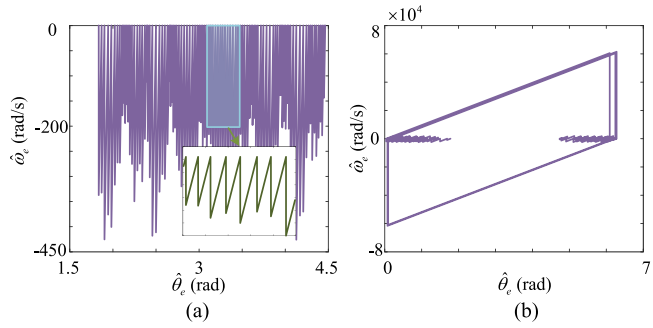


Fig. 4. Phase locus of the position and speed estimation obtained. (a) $\omega_{\text{PLL}} =$ 800 rad/s. (b) $\omega_{\text{PLL}} =$ 1200 rad/s.

To illustrate the limit cycle phenomenon in the position estimator, the phase locus of position and speed estimates is shown in Fig. 4, while the cases with different PLL parameter $\omega_{\text{PLL}}$ are compared. When $\omega_{\text{PLL}}$=800 rad/s, no autonomous oscillations happen, as shown in Fig. 3, and the phase locus presented in Fig. 4(a) has no closed trajectory in the phase space. It indicates no limit cycles in the control system. On the contrary, when the $\omega_{\text{PLL}}$=1200 rad/s, self-sustained oscillations are excited in the estimator, and a closed isolated curve can be found in the phase locus in Fig. 4(b). The closed trajectory is called the limit cycle.

The phase trajectory diagrams can also be obtained using the small-signal models analyzed in Fig. 2. As self-oscillation is not affected by external input, a minimal constant value is given as the input, and then compare the output results of the two models under the different PLL parameters. The comparative results are shown in Fig. 5.

As shown in Fig. 5, the nonlinear model considering speed errors has the same limit cycle phenomenon when the PLL parameter is selected to be higher. However, the linear model ignoring speed errors cannot reflect the limit cycle issues happening in the position-sensorless control system. In consequence, the conventional linear model, which is widely adopted in extended EMF-based sensorless control, is not accurate. The ignorance of speed errors results in inaccuracy modeling and long-time misunderstanding of autonomous issues in sensorless control.

## III. Analysis of the Nonlinear Model Based on Describing Function

### A. Equivalent Nonlinear Model for Describing Function Analysis

To identify the limit cycle in the position estimation of IPMSMs, a nonlinear analyzing approach, describing function method [35], is applied. The describing function method can effectively analyze the nonlinear system, which contains a linear part as well as one nonlinearity. The standard form of the closed-loop characteristic equation for a nonlinear system that can be analyzed by applying the describing function method is

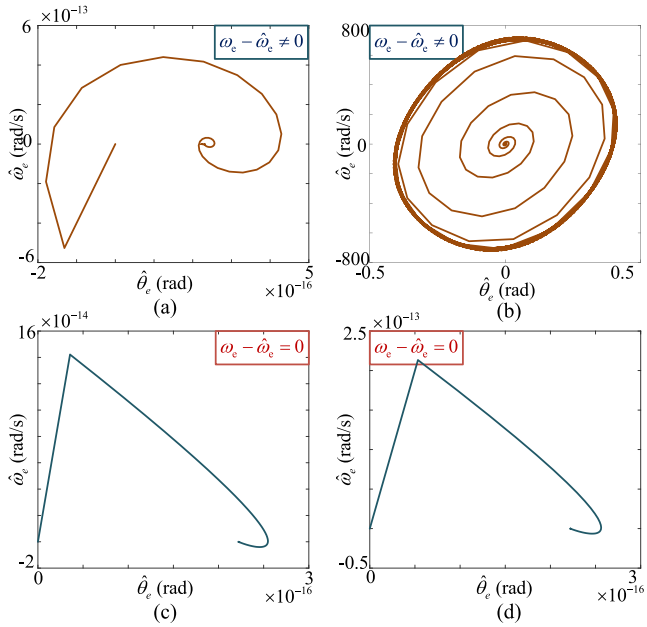


Fig. 5. Phase locus of the position and speed estimation obtained from two analytical models. (a) Nonlinear model with speed errors at $\omega_{\text{PLL}} = 800$ rad/s. (b) Nonlinear model with speed errors at $\omega_{\text{PLL}} = 1200$ rad/s. (c) Linear model ignoring speed errors at $\omega_{\text{PLL}} = 800$ rad/s. (b) Linear model ignoring speed errors at $\omega_{\text{PLL}} = 1200$ rad/s.

given by

$$1 + N(A) \cdot G(s) = 0 \tag{16}$$

where $N(A)$ is the describing function of the nonlinear part, and $G_{(s)}$ is the transfer function of the linear part. Therefore, to obtain the accurate equivalent model, the linear part and nonlinearity of the nonlinear model shown in Fig. 2(b) should be first separated. The open-loop transfer function $G_{\text{op}}(s)$ of the nonlinear model in Fig. 2(b) can be written as

$$\begin{aligned} G_{\text{op}}(s) &= [1 + m \cdot s \cdot N_{\text{arc}(A)}] \cdot G_{\text{pi}}(s)\frac{1}{s} \\ &= \frac{k_p s + k_i}{s^2} + m \cdot N_{\text{arc}}(A) \cdot \frac{k_p s + k_i}{s} \end{aligned} \tag{17}$$

where $G_{\text{pi}}(s) = k_p + \frac{k_i}{s}$ is the transfer function of the PI-controller, and $N_{\text{arc}(A)}$ is the describing function, which represents the frequency relationship between the first harmonic in the arctangent nonlinearity's output and a sinusoidal input with the magnitude $A$ [42].

According to the definition [42], $N_{\text{arc}(A)}$ can be calculated by

$$N_{\text{arc}}(A) = \frac{\int_0^{2\pi} \tan^{-1}(A \sin x) \sin x}{\pi A} dx = \frac{2(\sqrt{A^2+1} - 1)}{A^2}. \tag{18}$$

Based on the aforementioned equations, the close-loop characteristic equation for the nonlinear model can be simplified as

$$1 + G_{\text{op}}(s) = 1 + \frac{k_p s + k_i}{s^2} + m \cdot N_{\text{arc}}(A) \cdot \frac{k_p s + k_i}{s} = 0. \tag{19}$$

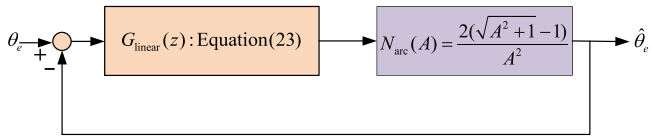


Fig. 6. Nonlinear model of the position estimator for describing function analysis.

To obtain an equivalent linear transfer function, (19) is reduced to a standard structure, where both sides of the equation are simultaneously divided by $Q = 1 + \frac{k_p s + k_i}{s^2}$, given as follows:

$$1 + G_{\text{op}}(s) = 1 + N_{\text{arc}}(A) \cdot \frac{ms(k_p s + k_i)}{s^2 + k_p s + k_i} = 0. \tag{20}$$

To separate the nonlinear model into linear and nonlinear parts, the characteristic equations of the original model and the equivalent model should be the same to keep the identical frequency characteristics, which results in

$$1 + G_{\text{op}}(s) = 1 + N_{\text{arc}}(A) G_{\text{linear}}(s). \tag{21}$$

Comparing (20) and (21), the transfer function of the linear part is given as follows:

$$G_{\text{linear}}(s) = \frac{ms(k_p s + k_i)}{s^2 + k_p s + k_i}. \tag{22}$$

Since the position estimator is implemented in the digital system with the sampling period $T_s$, the transfer function $G_{\text{linear}}(s)$ needs to be considered in the discrete form. In most cases, the Euler method offers good discretization accuracy and, thus, is widely used in the extended EMF-based estimator. For the integrator, its discrete form is $y[n] = y[n-1] + T_s u[n-1]$, and $y[n] = (u[n] - u[n-1])/T_s$ represents the discrete derivative, where $u[n]$ and $y[n]$ are the input and output signals at the $n$th sampling instant, respectively. After discretizing and adopting $z$-transformation, the discrete transfer function of the linear part can be obtained as

$$G_{\text{linear}}(z) = \frac{m(k_p z^2 + (k_i T_s - 2k_p)z - k_i T_s + k_p)}{z^3 + (k_p T_s - 2)z^2 + (k_i T_s^2 - k_p T_s + 1)z}. \tag{23}$$

As a result, by combining (18) and (23), the equivalent model for the nonlinear estimation model shown in Fig. 2(b) can be obtained in Fig. 6, where the model consists of linear and nonlinear parts in the discrete domain.

### B. Analysis of Autonomous Oscillation

Due to the arctangent nonlinearity caused by speed errors, the position estimator would have limit cycles, which excite the self-sustained oscillation in the position estimation. This self-oscillation is a periodic solution of the nonlinear system, which can be self-generated even though the input of the system is zero.

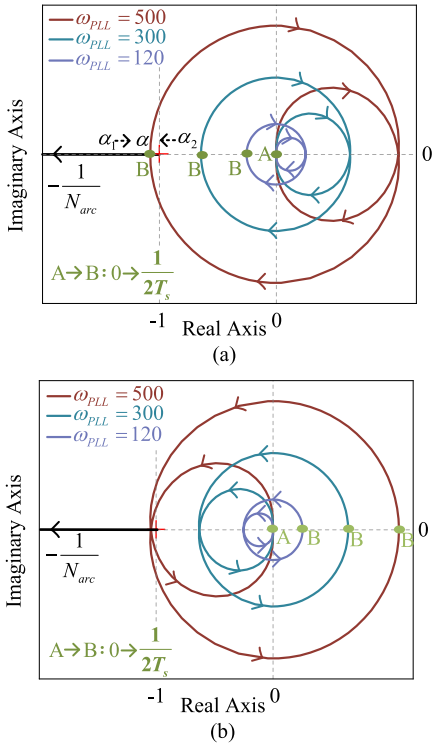


Fig. 7. Nyquist diagram of the position estimator. (a) $m$ is positive ($m = 0.001$), at the motoring mode. (b) $m$ is negative ($m = -0.001$), at the generating mode.

Hence, the periodic solution can be found by setting the characteristic (21) of the estimator to be zero, which gives

$$1 + N_{\text{arc}}(A)G_{\text{linear}}(z) = 0 \iff G_{\text{linear}}(z) = -\frac{1}{N_{\text{arc}}(A)} \tag{24}$$

where (24) indicates that the periodic solution of the nonlinear system is the intersection point of the linear part $G_{\text{linear}}(z)$ and the negative inverse of the describing function $-1/N_{\text{arc}}(A)$.

By substituting $z = e^{j\omega T_s}$ into (24), the Nyquist diagram of the linear part $G_{\text{linear}}(z)$ and the curve of $-1/N_{\text{arc}}(A)$ are plotted in Fig. 7. Here, both the cases with a positive $m$ (at the motoring mode)and negative $m$ (at the generating mode) are shown in Figs. 7(a) and (b), respectively.

As can be observed, there would be one crossover point $\alpha$ of the Nyquist curve and the curve of the negative inverse describing function regardless of the motor operating mode, if the PLL's parameter $\omega_{\text{PLL}}$ is set larger. According to the describing function theory [35], the crossover point $\alpha$ represents a stable self-sustained oscillation in Fig. 7(a). For example, when the amplitude A of the oscillation becomes large due to perturbance, the action point will move from $\alpha$ to $\alpha_1$, which departs from the surrounding of $G_{\text{linear}}(z)$, and the system remains stable. Therefore, the oscillation magnitude will reduce, and the action point will come back to $\alpha$. In contrast, when the oscillation magnitude decreases, the action point will move from $\alpha$ to $\alpha_2$. Due to the $\alpha_2$ being surrounded by $G_{\text{linear}}(z)$, the action point $\alpha_2$ is unstable, and the oscillation magnitude will increase. Finally, the action point moves back to $\alpha$ as well. The intersection point

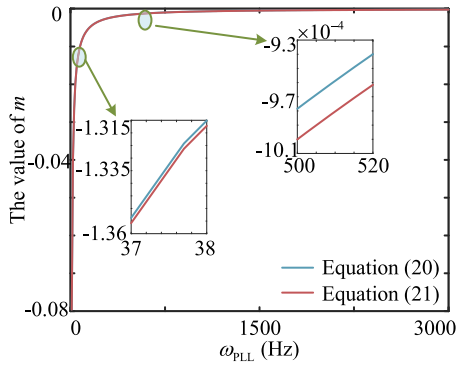


Fig. 8. Approximate $m$ and the critical $m$ with respect to $\omega_{\text{PLL}}$.

$\alpha$ indicates a stable self-sustained oscillation in the position estimator. According to Fig. 7, the $-1/N_{\text{arc}}(A)$ varies from $-1$ to negative infinity. Therefore, the critical condition of the autonomous oscillation is in the case when

$$G_{\text{linear}}(z) = -1. \tag{25}$$

By substituting $z = e^{j\omega T_s}$, (23), and PLL parameters (15) into (25) and solving the equation, the relationship between the variable $m$ and the PLL's parameter $\omega_{\text{PLL}}$ in the critical condition can be obtained as

$$m = \begin{cases} \dfrac{(-2 + T_s\omega_{\text{PLL}})^2}{2\omega_{\text{PLL}}(4 - T_s\omega_{\text{PLL}})}, & \text{if } m > 0 \\ \dfrac{-4 + 2T_s\omega_{\text{PLL}}}{\omega_{\text{PLL}}(\sqrt{9 - 4T_s\omega_{\text{PLL}}} - 2T_s\omega_{\text{PLL}} + 5)}, & \text{if } m < 0 \end{cases} \tag{26}$$

where two cases with positive $m$ and negative $m$ are given, respectively.

The bounded condition of the self-oscillation is related to $m$, which varies with the operating condition, as illustrated in (13), and the natural frequency $\omega_{\text{PLL}}$ of the PLL, if the sampling period $T_s$ of the digital system is fixed. When $m$ is positive, the motor runs in the motoring mode according to (13); when $m$ is negative, the motor operates in the generating mode. The two-mode operations have different bounded conditions, while $m$ should always be smaller than the critical values given in (26) to avoid self-oscillation.

To facilitate a simpler calculation of the bounded PLL parameter, the bounded condition (26) can be simplified by considering $T_s\omega_{\text{PLL}} \to 0$, as the sampling period is often a small value, which results in

$$|m| \approx \frac{1}{2\omega_{\text{PLL}}}. \tag{27}$$

Fig. 8 shows the difference between the approximate bounded criteria and the exact one. When $m$ is the same value, there is almost no difference between the exact bounded $\omega_{\text{PLL}}$ and the approximate one. However, the approximate condition given in (27) is simpler and would have more engineering significance.

To eliminate the autonomous oscillation phenomenon in sensorless control, the natural frequency of the PLL should satisfy

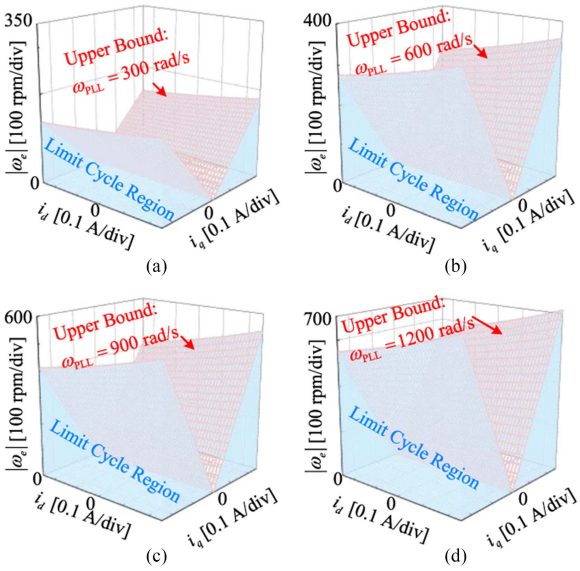


Fig. 9. Limit cycle region. (a) At $\omega_{\text{PLL}} = 300$ rad/s. (b) At $\omega_{\text{PLL}} = 600$ rad/s. (c) At $\omega_{\text{PLL}} = 900$ rad/s. (d) At $\omega_{\text{PLL}} = 1200$ rad/s.

the following approximate criterion:

$$\omega_{\text{PLL}} < \frac{1}{2|m|} = \left|\frac{\omega_e(\varphi - i_d \cdot \Delta L)}{2 i_q \cdot \Delta L}\right|. \tag{28}$$

In other words, the criteria (28) determines the maximum parameter of the PLL that can be used in the extended EMF-based IPMSM sensorless control.

To illustrate the criteria clearly, this article provides four cases with $\omega_{\text{PLL}} = 300, 600, 900, 1200$ rad/s to observe the limit cycle region under various operating conditions, and the results are shown in Fig. 9. The motor parameters are given in Table II in the experimental section. As the parameters of the PLL increase substantially, the area experiencing self-oscillation also expands. To stabilize the system, this phenomenon must be prevented. For Fig. 9(d), if the operating condition is on the surface where the upper bound of $\omega_{\text{PLL}}$ is equal to 1200 rad/s, self-sustained oscillations will be excited, causing significant position errors, as previously illustrated in Fig. 3. In contrast, as long as the operating conditions are not within the oscillation region, the rotor position can be well estimated without the limit cycle issue.

In summary, through the proposed nonlinear modeling and the autonomous oscillation analysis based on the describing function method, the maximum parameters of the PLL are obtained.

## IV. Experimental Validation

The analyses of autonomous oscillations in the extended EMF-based position estimation method are verified on an IPMSM setup, as shown in Fig. 10. Two identical IPMSMs are connected back-to-back with a common dc bus, which is powered by a dc power source. The sensorless control algorithm is executed on the RTU-BOX205 control unit with a frequency of 10 kHz. The machines are driven by an RTI-INV6010IR series inverter. Experimental data are recorded by Tektronix MD034 oscilloscope. The actual position and speed are measured by an encoder and used for observing the self-oscillations. The nominal motor parameters of the IPMSM drive are listed in Table II.

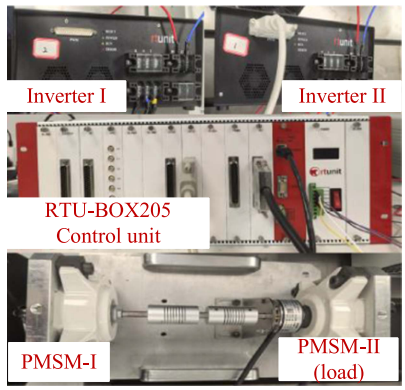


Fig. 10. IPMSM setup.

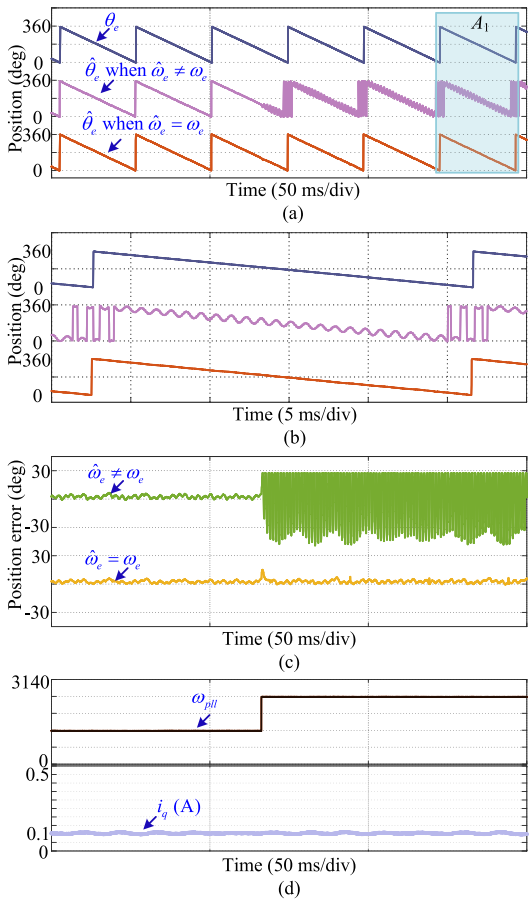


Fig. 11. Experimental verification of the criterion (28) accuracy at $-500$ r/min. (a) Estimated position from the different observers. (b) Enlarged area $A_1$. (c) Position error from the different observers. (d) Operating conditions.

Based on the analysis in this article, the criteria (28) must be satisfied to tune the parameter of the PLL. The accuracy of the criteria is verified by experiments, as shown in Fig. 11. The IPMSM runs at $-500$ r/min, and the reference values of $i_d$ and

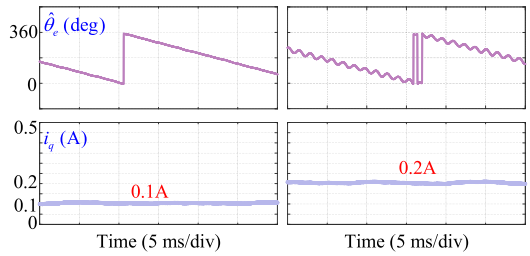


Fig. 12. $i_q$ effects on the criteria (28) at $-500$ r/min and $\omega_{\text{PLL}} = 1270$ rad/s.

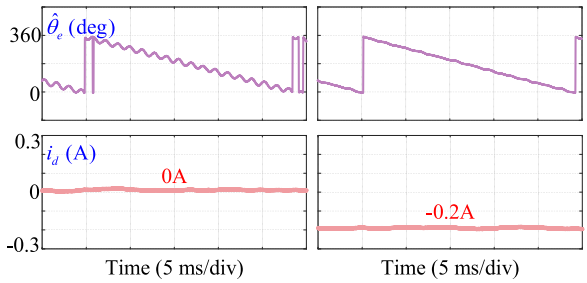


Fig. 13. Experimental validation of the critical criteria affected by $i_d$, at $-500$ r/min and $\omega_{\text{PLL}} = 1270$ rad/s.

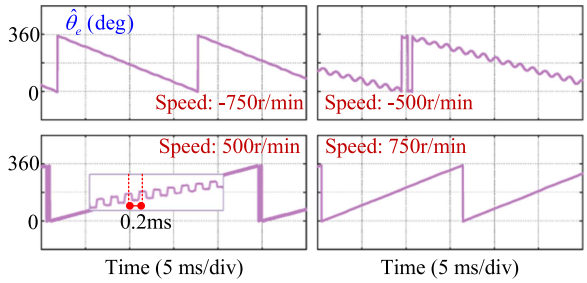


Fig. 14. Verification of critical criteria of the limit cycle issue in more operating conditions, at $\pm 750$ and $\pm 500$ r/min.

$i_q$ is equal to 0 and 0.1 A distinctly. In this operating condition, the critical $\omega_{\text{PLL}}$ that can excite the autonomous oscillation is 2525 rad/s. Two PLL's parameters, $\omega_{\text{PLL}} = 1270$ rad/s and $\omega_{\text{PLL}} = 2540$ rad/s, are set during the experiment to results from different observers, which use the actual speed test the oscillation phenomenon. The position estimation and the estimation speed as feedback to calculate the extended EMF, are shown in Figs. 10(b) and 11(a). When the $\omega_{\text{PLL}} = 1270$ rad/s, the position estimator does not reach the critical condition and the estimated position has no oscillations. To reach the boundary point, the $\omega_{\text{PLL}}$ increases to 2540 rad/s. Then, the estimated position using the estimated speed in the observer have self-sustained oscillations. However, the observer calculating the EMF using actual speed did not exhibit self-oscillation, indicating that the phenomenon is caused by errors in speed estimation. Thus, the proposed nonlinear model with speed errors in Section II is necessary to analyze the self-oscillation. Fig. 11(c) shows the position estimation errors when the PLL parameter changes between boundary values, which proves the limit cycle analyses in the widely used EMF-based sensorless control. Consequently, Fig. 11 shows that when the maximum value of $\omega_{\text{PLL}}$ in (28) is reached, due to the estimation speed error, the position observer would have self-oscillations. The parameter $\omega_{\text{PLL}}$ should be smaller than the maximum value.

### A. *Effects of $i_q$ on the Bounded Criteria*

The maximum value of the $\omega_{\text{PLL}}$ is related to the operating conditions. In this section, speed and $i_d$ are the same as Fig. 11, which are $-500$ r/min and 0 A, and the PLL parameter is a fixed value of 1270 rad/s. During the test, $i_q$ increases from 0.1 to 0.2 A. For the different values of $i_q$, the maximum values of $\omega_{\text{PLL}}$ are 2525 rad/s and 1262 rad/s. In Fig. 12, only the estimated position with speed errors is shown for a more convenient analysis. As can be seen, when $i_q = 0.1$ A, the critical value is not reached and there is no autonomous oscillation in the estimated position. However, when the $i_q$ is equal to 0.2 A and the fixed value 1270 rad/s exceeds the current critical value 1262 rad/s, the self-oscillation is generated in the position estimation and causes a large position error as shown in Fig. 12.

### B. *Effects of $i_d$ on the Bounded Criteria*

The critical criterion of the autonomous oscillation in position estimation can be affected by $i_d$. In the previous analysis, the $i_d$ has lower effects on the maximum value of $\omega_{\text{PLL}}$ compared with $i_q$ and speed. The $i_q$ is set to 0.2 A, and the speed is $-500$ r/min. When the motor is running, $i_d$ is set from 0 to $-0.2$ A. When $i_d$ is 0A, based on the Section IV-A, the critical PLL parameter $\omega_{\text{PLL}}$ is 1262 rad/s. In contrast, the maximum value is change to 1393 rad/s due to the increment of $i_d$, The value of the difference between the two critical points is smaller than the effects from $i_q$. In Fig. 13, $\omega_{\text{PLL}}$ is set to 1270 rad/s. Before the change of $i_d$, $\omega_{\text{PLL}}$ is larger than the critical point 1262 rad/s, and the limit cycle occurs. When the critical point is increased by changing the value of $i_d$, the self-oscillation disappears. Even the variance of the critical value is smaller, the effects on the estimation position cannot be ignored. Consequently, the critical criterion is practical and can be used to predict the self-oscillations in the extended EMF-based sensorless control.

### C. *Effects of $\omega_e$ and $m$ on the Bounded Criteria*

According to the analysis of (26), whether $m$ is positive or negative would cause differences on the critical point.

Equation (28) is an appropriate result; however, it is accurate and practical, which is verified by the above experiments. For further verification, the sign of $m$ is determined by the direction of speed, and the different speed values are set during the test. The $i_d$ and $i_q$ are set to 0 and 0.2 A, respectively. In Fig. 14, $\omega_{\text{PLL}}$ is set to 1270 rad/s. When the speed is $-750$ r/min, the critical point of $\omega_{\text{PLL}}$ for limit cycle is 1893 rad/s and is larger than the given $\omega_{\text{PLL}}$. There are no self-oscillations. With the decrease of speed, the critical point is changed as 1262 rad/s. The self-oscillations are derived, and the frequency is about 600 Hz. Besides the validation at the negative speed given in Fig. 14, the accuracy of the critical criterion in the positive speed

is also verified. Based on (28), in the identical operating conditions, the critical points of −500 and 500 r/min are the same, 1262 rad/s. The maximum at 700 r/min is also the same as at −700 r/min, 1893 rad/s. For the positive speed, the phenomenon is similar to the negative speed. When the $\omega_{\text{PLL}}$ exceeds the critical point, the self-oscillation could be observed. However, the HF oscillation is derived, from about 5 kHz, not 600 Hz. Based on Fig. 7, the phenomenon is reasonable. The direction of the speed leads to the sign of $m$. In Fig. 7, the frequency is high at (−1,0) when $m$ is positive, and the intersection with the negative real axis in Fig. 7(a) is half of the control period. Therefore, the value of the frequency is 5 kHz. The positive value of $m$ leads to a higher frequency oscillation compared with the negative value.

In summary, the accuracy of the proposed nonlinear model for extended EMF-based sensorless control is verified by the experiments and can be applied to determine the boundary parameters of the PLL. The maximum $\omega_{\text{PLL}}$ of the PLL should be smaller than the critical criterion in order to avoid autonomous oscillation in sensorless control.

## V. Conclusion

In this article, a serious autonomous oscillation issue is found in the widely used extended EMF-based position estimation method for IPMSM drives. This issue is caused by the speed estimation error in the position estimator, which results in an arctangent nonlinearity in the feedforward path. Since conventional observer design methods are based on a linear model, they cannot reflect the nonlinearity characteristic of the estimator. To investigate the self-sustained oscillation problem in the position estimation, a nonlinear model of the extended EMF-based estimator is built, and the critical criteria are derived through the describing function method. The results show that the parameters of the PLL should be smaller than the maximum values, which are related to the operating conditions and motor parameters. Finally, the correctness of the theoretical analysis is verified by experimental tests on an IPMSM setup.

For future work, 1) the classic EMF model would be further improved to find the method that can avoid the limit cycle issue. 2) Other estimation-based performance would be observed to determine whether there is a limit cycle issue, and detailed analyses should be presented. 3) The impact of parameter mismatch on the analysis results needs to be further considered. 4) The oscillation's frequency would be accurately identified, and the influence of the limit cycle issue considering speed errors can be removed.

## References


[1] H. Jing et al., "Gradient boosting decision tree for rotor temperature estimation in permanent magnet synchronous motors," *IEEE Trans. Power Electron.*, vol. 38, no. 9, pp. 10617–10622, Sep. 2023.

[2] G. Wang, M. Valla, and J. Solsona, "Position sensorless permanent magnet synchronous machine drives—A review," *IEEE Trans. Ind. Electron.*, vol. 67, no. 7, pp. 5830–5842, Jul. 2020.

[3] X. Wang et al., "Optimization-basedparameter estimation for PMSMS under unified observable conditions," *IEEE Trans. Power Electron.*, vol. 39, no. 2, pp. 2632–2643, Feb. 2024.

[4] N. Zhao, G. Wang, D. Xu, L. Zhu, G. Zhang, and J. Huo, "Inverter power control based on DC-link voltage regulation for IPMSM drives without electrolytic capacitors," *IEEE Trans. Power Electron.*, vol. 33, no. 1, pp. 558–571, Jan. 2018.

[5] C.-E. Hwang, Y. Lee, and S.-K. Sul, "Analysis on position estimation error in position-sensorless operation of IPMSM using pulsating square wave signal injection," *IEEE Trans. Ind. Appl.*, vol. 55, no. 1, pp. 458–470, Jan./Feb. 2019.

[6] S.-C. Yang, S.-M. Yang, and J.-H. Hu, "Design consideration on the square-wave voltage injection for sensorless drive of interior permanent-magnet machines," *IEEE Trans. Ind. Electron.*, vol. 64, no. 1, pp. 159–168, Jan. 2017.

[7] G. Wang, R. Liu, N. Zhao, D. Ding, and D. Xu, "Enhanced linear ADRC strategy for HF pulse voltage signal injection-based sensorless IPMSM drives," *IEEE Trans. Power Electron.*, vol. 34, no. 1, pp. 514–525, Jan. 2019.

[8] P. Xu and Z.-Q. Zhu, "Novel square-wave signal injection method using zero-sequence voltage for sensorless control of PMSM drives," *IEEE Trans. Ind. Electron.*, vol. 63, no. 12, pp. 7444–7454, Dec. 2016.

[9] G. Zhang, G. Wang, H. Wang, D. Xiao, L. Li, and D. Xu, "Pseudorandom-frequency sinusoidal injection based sensorless IPMSM drives with tolerance for system delays," *IEEE Trans. Power Electron.*, vol. 34, no. 4, pp. 3623–3632, Apr. 2019.

[10] Y. Zhang, Z. Yin, C. Du, J. Liu, and X. Sun, "Noise spectrum shaping of random high-frequency-voltage injection based on Markov chain for IPMSM sensorless control," *IEEE Trans. Emerg. Sel. Topics Power Electron.*, vol. 8, no. 4, pp. 3682–3699, Dec. 2020.

[11] D. Luo, H. Ji, Z. Chen, X. Wang, and D. Xiao, "Audible noise and EMI mitigation in IPMSM zero or low-speed sensorless drive with randomized low-frequency pulse voltage injection," *IEEE Trans. Transp. Electrific.*, early access, Jul. 3, 2024, doi: 10.1109/TTE.2024.3422685.

[12] J. Wang, K. Hu, Y. Bo, F. Wang, and J. Rodríguez, "Position sensorless control strategy based on an enhanced high order generalized integrator flux observer for PMSM drives," *IEEE Trans. Power Electron.*, vol. 39, no. 10, pp. 12910–12924, Oct. 2024.

[13] A. T. Woldegiorgis, X. Ge, H. Wang, and Y. Zuo, "An active flux estimation in the estimated reference frame for sensorless control of IPMSM," *IEEE Trans. Power Electron.*, vol. 37, no. 8, pp. 9047–9060, Aug. 2022.

[14] S. Wang et al., "Adaptive position estimation error suppression method based on limit cycle oscillator for sensorless PMSM drives," *IEEE Trans. Power Electron.*, vol. 39, no. 11, pp. 14939–14950, Nov. 2024.

[15] G. Wang, R. Yang, and D. Xu, "DSP-based control of sensorless IPMSM drives for wide-speed-range operation," *IEEE Trans. Ind. Electron.*, vol. 60, no. 2, pp. 720–727, Feb. 2013.

[16] T. Wu, X. Wu, S. Huang, K. Lu, and H. Cui, "An optimized PLL with time delay and harmonic suppression for improved position estimation accuracy of PMSM based on Levenberg–Marquardt," *IEEE Trans. Ind. Electron.*, vol. 70, no. 10, pp. 9847–9858, Oct. 2023.

[17] S. Zhou, K. Liu, W. Hu, D. Zhang, C. Huang, and Y. Chen, "Inverter harmonic suppression for permanent magnet synchronous machine drives based on discontinuous SVPWM with variable switching frequency," *IEEE Trans. Transport. Electrific.*, vol. 9, no. 2, pp. 2419–2428, Jun. 2023.

[18] G. Zhang, G. Wang, D. Xu, and N. Zhao, "ADALINE-network-based PLL for position sensorless interior permanent magnet synchronous motor drives," *IEEE Trans. Power Electron.*, vol. 31, no. 2, pp. 1450–1460, Feb. 2016.

[19] X. Wu et al., "Enhanced position sensorless control using bilinear recursive least squares adaptive filter for interior permanent magnet synchronous motor," *IEEE Trans. Power Electron.*, vol. 35, no. 1, pp. 681–698, Jan. 2020.

[20] S. Chen, X. Wu, J. Chen, G. Tan, and Y. Wang, "Second-order lead compensator-based quadrature PLL for sensorless interior permanent magnet synchronous motor control," *IET Power Electron.*, vol. 13, no. 3, pp. 568–575, 2020.

[21] D. Xiao et al., "Computation-efficient position estimation algorithm for permanent magnet synchronous motor drives under distorted conditions," *IEEE Trans. Emerg. Sel. Topics Power Electron.*, vol. 9, no. 3, pp. 2759–2773, Jun. 2021.

[22] L. Wang, Z.-Q. Zhu, H. Bin, and L. Gong, "Current harmonics suppression strategy for PMSM with nonsinusoidal back-EMF based on adaptive linear neuron method," *IEEE Trans. Ind. Electron.*, vol. 67, no. 11, pp. 9164–9173, Nov. 2020.

[23] T. Liu, Z.-Q. Zhu, B. Shuang, Z.-Y. Wu, D. A. Stone, and M. P. Foster, "An online position error correction method for sensorless control of permanent magnet synchronous machine with parameter mismatch," *IEEE Access*, vol. 9, pp. 135708–135722, 2021.
[24] S. Bolognani, S. Calligaro, and R. Petrella, "Design issues and estimation errors analysis of back-EMF-based position and speed observer for SPM synchronous motors," *IEEE Trans. Emerg. Sel. Topics Power Electron.*, vol. 2, no. 2, pp. 159–170, Jun. 2014.
[25] S. Bolognani, L. Ortombina, F. Tinazzi, and M. Zigliotto, "Model sensitivity of fundamental-frequency-based position estimators for sensorless PM and reluctance synchronous motor drives," *IEEE Trans. Ind. Electron.*, vol. 65, no. 1, pp. 77–85, Jan. 2018.
[26] M. S. Rafaq, F. Mwasilu, J. Kim, H. H. Choi, and J.-W. Jung, "Online parameter identification for model-based sensorless control of interior permanent magnet synchronous machine," *IEEE Trans. Power Electron.*, vol. 32, no. 6, pp. 4631–4643, Jun. 2017.
[27] T. Wang et al., "An EMF observer for PMSM sensorless drives adaptive to stator resistance and rotor flux linkage," *IEEE Trans. Emerg. Sel. Topics Power Electron.*, vol. 7, no. 3, pp. 1899–1913, Sep. 2019.
[28] Y. Shi, K. Sun, L. Huang, and Y. Li, "Online identification of permanent magnet flux based on extended Kalman filter for IPMSM drive with position sensorless control," *IEEE Trans. Ind. Electron.*, vol. 59, no. 11, pp. 4169–4178, Nov. 2012.
[29] P. Xu and Z.-Q. Zhu, "Carrier signal injection-based sensorless control for permanent-magnet synchronous machine drives considering machine parameter asymmetry," *IEEE Trans. Ind. Electron.*, vol. 63, no. 5, pp. 2813–2824, May 2016.
[30] L. Wu, Z. Lyu, Z. Chen, J. Liu, and Y. Lu, "An enhanced sensorless control scheme for PMSM drives considering self-inductance asymmetry," *CES Trans. Elect. Machines Syst.*, vol. 6, no. 4, pp. 384–392, 2022.
[31] G. Wang, H. Zhan, G. Zhang, X. Gui, and D. Xu, "Adaptive compensation method of position estimation harmonic error for EMF-based observer in sensorless IPMSM drives," *IEEE Trans. Power Electron.*, vol. 29, no. 6, pp. 3055–3064, Jun. 2014.
[32] J. Kim, I. Jeong, K. Nam, J. Yang, and T. Hwang, "Sensorless control of PMSM in a high-speed region considering iron loss," *IEEE Trans. Ind. Electron.*, vol. 62, no. 10, pp. 6151–6159, Oct. 2015.
[33] S.-C. Yang and G.-R. Chen, "High-speed position-sensorless drive of permanent-magnet machine using discrete-time EMF estimation," *IEEE Trans. Ind. Electron.*, vol. 64, no. 6, pp. 4444–4453, Jun. 2017.
[34] Y. Lee and S.-K. Sul, "Model-based sensorless control of an IPMSM with enhanced robustness against load disturbances based on position and speed estimator using a speed error," *IEEE Trans. Ind. Appl.*, vol. 54, no. 2, pp. 1448–1459, Mar./Apr. 2018.
[35] O. Fendrich, "Describing functions and limit cycles," *IEEE Trans. Autom. Control*, vol. 37, no. 4, pp. 486–487, Apr. 1992.
[36] S.-C. Yang and Y.-L. Hsu, "Full speed region sensorless drive of permanent-magnet machine combining saliency-based and back-EMF-based drive," *IEEE Trans. Ind. Electron.*, vol. 64, no. 2, pp. 1092–1101, Feb. 2017.
[37] S. Wang, H. Wang, C. Tang, J. Li, D. Liang, and Y. Qu, "Research on control strategy of permanent magnet synchronous motor based on fast terminal super-twisting sliding mode observer," *IEEE Access*, vol. 12, pp. 141905–141915, 2024.
[38] S. Wang et al., "Sensorless control strategy for permanent magnet synchronous motor based on adaptive non-singular fast terminal sliding mode observer," *IEEE Trans. Appl. Supercond.*, vol. 34, no. 8, Nov. 2024, Art. no. 5208905.
[39] G. Xu, F. Xiao, and C. Lian, "A position sensorless control strategy for PMSM drives with single phase current sensor," *IEEE Trans. Transport. Electrific.*, vol. 10, no. 3, pp. 4678–4688, Sep. 2024.
[40] Z. Chen et al., "General-purpose high-speed position-sensorless control of switched reluctance motors using single-phase adaptive observer," *IEEE Trans. Transport. Electrific.*, vol. 10, no. 3, pp. 5241–5249, Sep. 2024.
[41] D. Bao, X. Pan, Y. Wang, X. Wang, and K. Li, "Adaptive synchronous-frequency tracking-mode observer for the sensorless control of a surface PMSM," *IEEE Trans. Ind. Appl.*, vol. 54, no. 6, pp. 6460–6471, Nov./Dec. 2018.
[42] R. Sridhar, "A general method for deriving the describing functions for a certain class of nonlinearities," *IRE Trans. Autom. Control*, vol. 5, no. 2, pp. 135–141, 1960.

**Xinghao Wang** (Graduate Student Member, IEEE) received the B.S. and M.S. degrees in automation and control science and control engineering from the Northeastern University, Shenyang, China, in 2019 and 2022, respectively. He is currently working toward the Ph.D. degree in sustainable energy and environment with The Hong Kong University of Science and Technology (Guangzhou), Guangzhou, China.

His research interests include electric drivers and control techniques, control science, and control engineering, particularly in the application of electrified transportation.

**Dehui Luo** (Graduate Student Member, IEEE) received the B.S. degree in electrical engineering from the University of British Columbia, Vancouver, BC, Canada, in 2021. He is currently working toward the M.Phill. degree in sustainable energy and environment with The Hong Kong University of Science and Technology (Guangzhou), Guangzhou, China.

His research interests include electric drive and control, particularly in the application of electrified transportation.

**Dianxun Xiao** (Member, IEEE) received the B.E. and M.E. degrees in electrical engineering from the Harbin Institute of Technology, Harbin, China, in 2016 and 2018, respectively, and the Ph.D. degree in electrical and computer engineering from McMaster University, Hamilton, ON, Canada, in 2021.

He is currently an Assistant Professor with the Sustainable Energy and Environment Thrust, The Hong Kong University of Science and Technology (Guangzhou), Guangzhou, China. He is also with The Hong Kong University of Science and Technology, Clear Water Bay, Hong Kong. In 2021, he was a Postdoctoral Research Fellow with McMaster Automotive Resource Centre, McMaster University, Hamilton, ON, Canada. His research interests include permanent magnet synchronous motor drives, switched reluctance motor drives, high-power converters, and battery management systems for transportation electrification applications.

Dr. Xiao is an Associate Editor for IEEE TRANSACTIONS ON TRANSPORTATION ELECTRIFICATION. He was the recipient of IEEE Myron Zucker Student-Faculty grant in 2024.